Improved SA Turbulence Model For Hovering Rotor Using Production Limiter

Yoonpyo Hong
Research Engineer
German Aerospace Center (DLR)
Braunschweig, Germany

Walid Khier
Research Engineer
German Aerospace Center (DLR)
Braunschweig, Germany

Gunther Wilke
Research Engineer
German Aerospace Center (DLR)
Braunschweig, Germany

ABSTRACT

The simulation of hovering rotorcraft flow continues to present formidable challenges in computational fluid dynamics, owing to its intrinsically unsteady characteristics and the complexity of rotor wake vortex interactions. Conventional turbulence models such as the Spalart-Allmaras (SA) model face difficulties in accurately capturing rotor wake structures, often resulting in excessive vortex dissipation. This study proposes a production limiter for the SA model to address the over-production of turbulent eddy viscosity in wake regions. The limiter incorporates a shielding function from the delayed detached eddy simulation formulation to preserve the original SA model behavior within boundary layers while targeting outer wake regions. Validation through turbulent flat plate and transonic airfoil test cases demonstrates that the production limiter maintains boundary layer prediction accuracy while effectively controlling turbulent eddy viscosity in wake regions. Application to the HVAB rotor shows significant improvements in vortex preservation and aerodynamic performance prediction with minimal computational overhead.

INTRODUCTION

Despite remarkable advances in computing power and numerical algorithms, the simulation of rotorcraft flow remains a formidable challenge. In particular, while hovering flight appears deceptively simple to simulate, its inherently unsteady characteristics such as secondary vortex structures renders it one of the most challenging problems in the rotorcraft community. The presence of strong vortices and complex vortex-body interactions introduces significant difficulties in both physical understanding and numerical simulations. Computational fluid dynamics (CFD) analyses of rotorcraft have evolved considerably over the years, transitioning from steady-state solvers with limited grid resolutions to high-fidelity, scale-resolving unsteady simulations. However, even though these advancements have been achieved, conventional turbulence models such as the Spalart-Allmaras (SA) model continue to face challenges in accurately capturing rotor wake structures, often leading to excessive vortex dissipation. This dissipated vortex structure consequently becomes one of the primary causes of drag over-prediction (Ref. 1).

One major cause of the highly dissipative characteristics of the SA model is the excessive production of turbulent eddy viscosity (TEV) in the wake region. In particular, this over-production is notably evident in the results of steady solvers, which assume steady-state solutions and advance the pseudo-time rapidly. Figure 1 illustrates this phenomenon. The converged steady solution appears to be extremely dissipative compared to the unsteady solution with 50 revolutions. TEV increases unboundedly and destroys the vortex structures in the steady case. In contrast, the tip vortex trajectory can be clearly observed in the unsteady case, as the TEV has not yet been produced excessively. If the simulation proceeds for additional revolutions, the TEV of the unsteady solution also eventually becomes unbounded. The solutions are generated using a CFD software by ONERA, DLR, and Airbus (CODA) (Ref. 2). Comparable results are also observed with conventional finite volume based solvers such as FLOWer (Ref. 3), elSA (Ref. 4), and KFLOW (Refs. 5, 6).

To address this over-production of TEV in the wake region, various corrections to the model have been introduced, including rotation-curvature corrections (Refs. 7, 8) and detached eddy simulation (DES) variants (Refs. 1, 9–11). These approaches show promising results in multiple scenarios, including unsteady rotor simulations and steady wing tip vortex preservation. However, these methods still encounter difficulties in fully resolving the hovering flow problem, particularly in steady cases, leading to persistent vortex dissipation and erroneous aerodynamic predictions. Converged steady solutions using these techniques are shown in Fig. 2.

A significant challenge in the widely used SA turbulence model lies in its original formulation, which was designed primarily for attached boundary layers over turbulent flat plates and airfoils. Specifically, the destruction term in the SA equation depends on the wall distance, leading to an imbalance in the production of eddy viscosity in wake region regions. Over extended simulation times, this imbalance results in excessive TEV, adversely impacting flow predictions. An engineering approach involving a laminar off-body model has been explored (Refs. 12, 13). This approach effectively suppresses the generation of TEV in the off-body region by removing the source terms exclusively in the off-body region. However, while this method is practical for engineering purposes, it presents certain theoretical considerations due to variations

Presented at the 51th European Rotorcraft Forum.

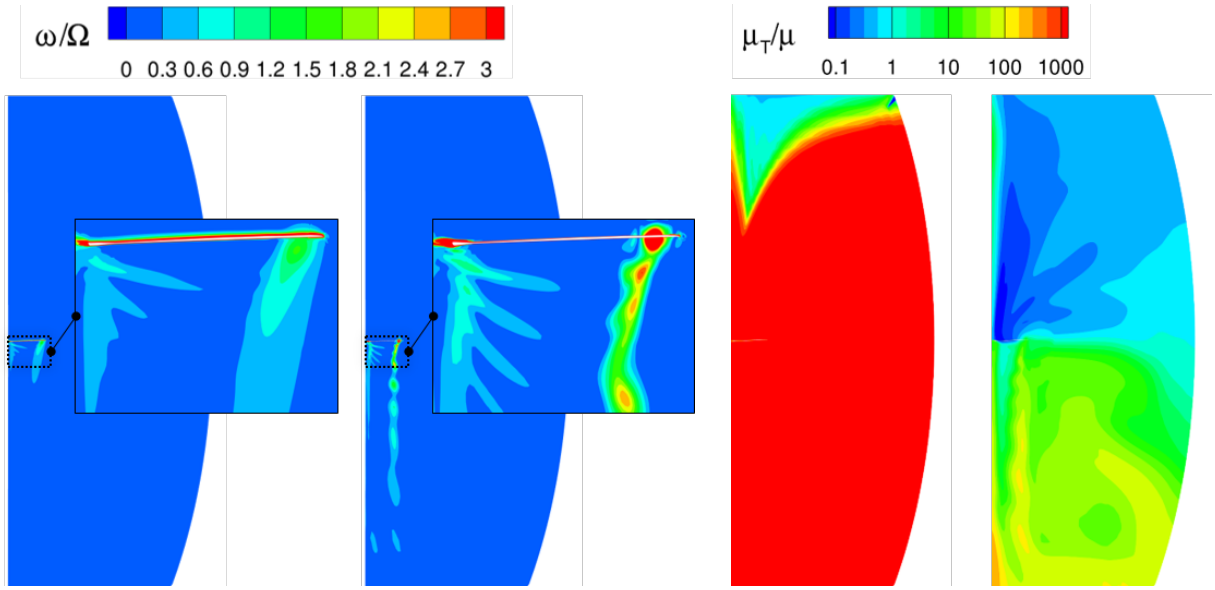

(a) Vorticity contour, (left: steady, right: unsteady) (b) TEV contour, (left: steady, right: unsteady)

Figure 1. An example of hovering solutions of HVAB rotor with $\theta = 10^{\circ}$. Converged steady solution shows highly dissipative vorticity contour due to the unbounded increase of TEV. On the other hand, unsteady solution with 50 revolutions shows enhanced vorticity preservability and TEV field.

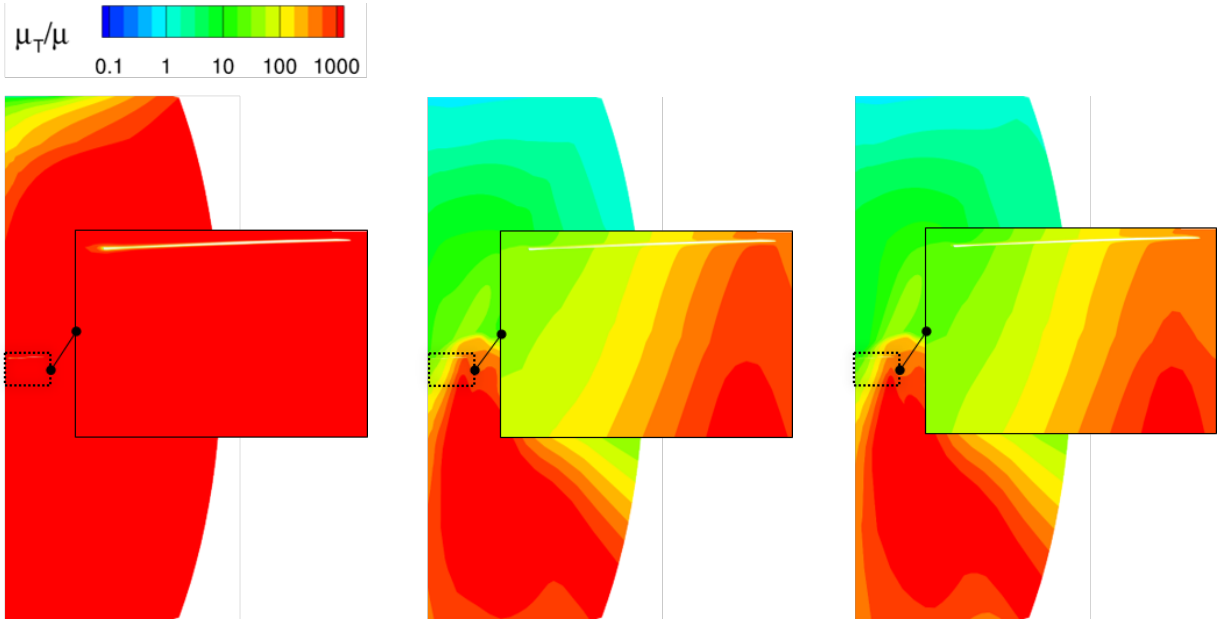

(a) SA-neg-R95 (b) SA-neg-DDES (c) SA-neg-R95-DDES

Figure 2. Other possible solutions for mitigating the increase of TEV.

in the governing equation depending on the domain.

Therefore, a modified version of the SA model is proposed in this study to address the aforementioned issues for hovering rotorcraft flows. By conducting a detailed analysis of the terms in the SA model, a production limiter is newly proposed to prevent excessive growth of the TEV. The proposed limiter is designed to target only the outer region by employing a shielding function, thereby preserving the original formulation of the SA model within the boundary layer. The modified SA model employing this limiter is validated through turbulent flat plate and transonic airfoil cases, demonstrating its accuracy and robustness. Subsequently, it is applied to the hover validation and acoustic baseline (HVAB) rotor (Refs. 14, 15) under turbulent conditions, demonstrating significant improvements in vortex preservation and numerical stability with minimal computational overhead. The fol-

lowing sections include a brief description of the SA model, introduction of the production limiter, numerical experiments and results of the new model, and conclusions.

ANALYSIS OF THE ORIGINAL SA MODEL

Spalart-Allmaras turbulence equation

The original SA turbulence equation (Ref. 16) is a transport equation for the SA variable ($\tilde{\nu}$). The equation can be written as follows:

$$\frac{\partial \tilde{\nu}}{\partial t} + u_j \frac{\partial \tilde{\nu}}{\partial x_j} = Prod. - Dest. + Diff. \tag{1}$$

$$\mu_t = \rho \tilde{\nu} f_{v1} \tag{2}$$

where $Prod.$, $Dest.$, and $Diff.$ refer to production, destruction, and diffusion terms, respectively.

The SA variable $\tilde{\nu}$ behaves identically to ν_t except in the viscous region. Spalart and Allmaras introduced f_{v1} to ensure linear behavior near the wall region, which consequently requires fewer grid points near the wall than an algebraic turbulence model. The source terms of the SA model, similar to other turbulence equations, consist of production, destruction, and diffusion terms. Through these source terms, $\tilde{\nu}$ is either generated or dissipated, achieving a balanced solution. Details of the source terms can be found in (Ref. 16). The production term increases in proportion to both the magnitude of vorticity and $\tilde{\nu}$. Consequently, in hovering flow where vortices remain near the rotor blade, the production term continuously supplies $\tilde{\nu}$. In contrast, the destruction term increases in proportion to the square of $\tilde{\nu}$ but is inversely proportional to the square of the wall distance. This implies that near the wall, the destruction term can adequately balance the production term. However, in the wake region, as the wall distance increases, the destruction term may diminish in magnitude, potentially reducing its effectiveness.

Behavior of the source terms in hovering flow fields

Highly unsteady and complex vortices are actively generated by the rotor blade and convected downward axially under hovering conditions. In contrast to the relatively high speed of the blade tip section, the inflow velocity is very low, resulting in an accumulated vortex field near the rotor disk. Due to this inherent characteristic of hovering flow fields, substantial amounts of TEV are produced and accumulated near the rotor blade.

Considering that the SA variable is a slightly modified form of TEV (Eq. 2), it can be noted that TEV is primarily produced by the production term and destroyed by the destruction term of the SA equation. The production and destruction terms can be written as follows:

$$Prod. = c_{b1}(1 - f_{t2})\tilde{S}\tilde{\nu} \tag{3}$$

$$Dest. = \left[c_{w1} f_w - \frac{c_{b1}}{\kappa^2} f_{t2}\right] \left(\frac{\tilde{\nu}}{d}\right)^2 \tag{4}$$

where $Prod.$ and $Dest.$ indicate the production and destruction term, respectively. $\tilde{S}$ is a modified vorticity, and d is the distance from the wall. Details of the functions and coefficients in Eqs. 3 and 4 can be found in (Refs. 16, 17).

Due to $\tilde{S}$ in the production term, TEV is continuously produced in the wake region where tip vortices of high $\tilde{S}$ exist. On the other hand, the destruction term cannot be increased beyond a certain distance from the wall because of d. Considering that the production term has a linear relationship with $\tilde{\nu}$, once $\tilde{\nu}$ increases for any reason in the wake region, interrupting the production of TEV presents significant challenges.

Assuming a hovering flow field with a vorticity magnitude (ω) of 1.0 $\times$ angular velocity (Ω), the trends of both terms in the original SA model (Ref. 16) can be represented in Fig. 3. Two regions are considered for comparison: Fig. 3a represents a near-wall region where $d = 0.072c$, and Fig. 3b represents a wake region where $d = 7.2c$. c is a mean chord length of the

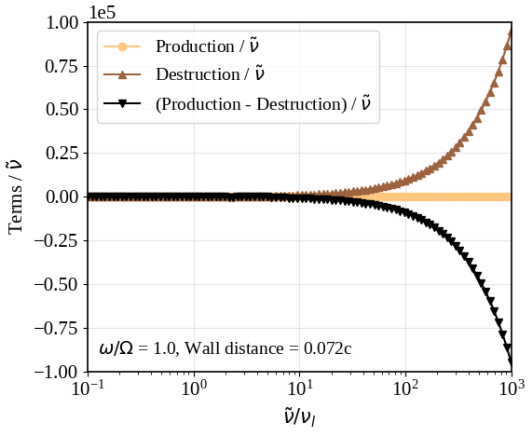

(a) Near wall region (wall distance = 0.072c)

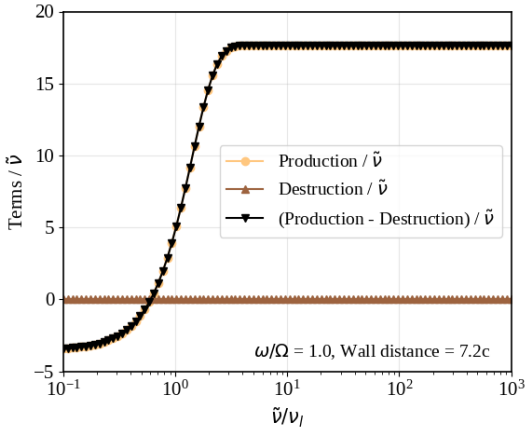

(b) Wake region (wall distance = 7.2c)

Figure 3. Trend of SA source terms in two regions: a) near wall, and b) wake region of an isolated rotor in hover.

blade. The horizontal axis represents the SA variable normalized by dynamic viscosity (μ_l). In the near-wall region, the destruction term has a larger value than the production term when the normalized SA variable exceeds 10. In this manner, TEV can be balanced within an appropriate range. However, in the wake region, the destruction term is severely limited due to the large value of d, while the production term remains active with large values. Therefore, if the simulation continues until a converged state is reached, the amount of produced TEV becomes unbounded, yielding a highly dissipated solution.

DEVELOPMENT OF THE PRODUCTION LIMITER

Production limiter formulation

A limiter for the production term is newly proposed in this study to mitigate the aforementioned problem. The new form of limiter suppresses the growth of the production term to a ratio of the destruction term as follows:

$$Prod._{limited} = \min(Prod.,\ c_1 \times Dest.) \tag{5}$$

where c_1 is the ratio of production to destruction. By limiting the production term to a ratio of the destruction term, unnecessary production of TEV can be avoided in the wake region, and the destruction term can play an effective role even in the wake region.

However, this limiter in its rather simple form can deteriorate convergence and robustness by limiting production within the boundary layer if the ratio (c_1) is set too low. Considering that the wake region far from the solid surface experiences the TEV problem, it is essential to target the specific region that should be limited. A shielding function from the delayed DES (DDES) formulation (Ref. 9) provides a favorable solution for targeting the region, since it distinguishes the boundary layer region from the entire domain. Therefore, the advanced form of the production limiter incorporating the shielding function can be expressed as follows:

$$Prod._{limited} = Prod. - f_d \times \min(0, Prod. - c_1 \times Dest.) \tag{6}$$

$$f_d = 1 - \tanh\left([c_2 r_d]^3\right) \tag{7}$$

$$r_d = \frac{\nu_t + \nu}{\sqrt{U_{i,j}U_{i,j}}\kappa^2 d^2} \tag{8}$$

where f_d and r_d are the shielding functions borrowed from the original DDES formulation (Ref. 9). f_d is designed to approach 0 within the boundary layer and 1 in the outer region where $r_d << 1$. Thus, f_d functions as a smooth transition function for the production limiter that can be activated only in the outer region.

Two constants in Eqs. 6 and 7, c_1 and c_2, are determined as 100 and 20, respectively, based on numerical experiments including flat plate, various airfoil shapes, and hovering rotor configurations. c_1, the ratio of production term to destruction term, was tested from 5 to 10^{10}. The stable range varies from case to case, but $c_1 = 100$ ensures both accuracy and robustness for hovering flow fields. c_2 is the constant for the f_d term that directly affects the shielding region. It was originally suggested to be 8 in Spalart et al's research (Ref. 9) and further investigated by researchers for their applications in various engineering fields (Refs. 18, 19). Considering that a larger value of c_2 guarantees a larger area of shielding, c_2 is determined as 20 for robustness. Further investigation and details regarding c_1 and c_2 will be presented in a later section.

Validation of the modified SA model

Two different cases are selected for the validation of the modified SA model with the newly defined production limiter. The purpose is to verify whether this production limiter affects the wall boundary layer behavior. Since the limiter is designed to preserve the original formulation within the boundary layer by adopting the shielding function concept, the SA model without the production limiter is also employed for comparison.

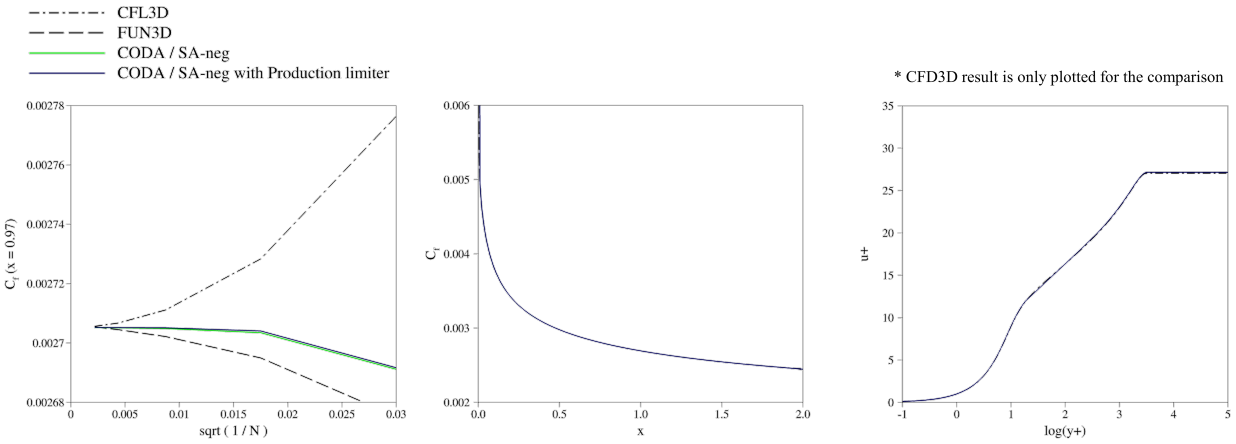

(a) Grid convergence plot for skin friction at x=0.97 (b) Skin friction coefficient on the finest grid (c) Boundary layer profile at x=0.97 on the finest grid

Figure 4. Validation results on turbulent flat plate which has a Mach number of 0.2 and a Reynolds number of 5 million.

Solver details The CFD solver used in this research is CODA, a CFD software developed as part of a collaboration between the French Aerospace Lab ONERA, the German Aerospace Center (DLR), Airbus, and their European research partners (Ref. 2). CODA is jointly owned by ONERA, DLR, and Airbus. The presented production limiter is evaluated using the latest version (2025.05) of CODA. For the two validation cases, same numerical settings are applied: For the gradient computation of convective flux, the node-based extended Green-Gauss method (Refs. 2, 20) with second-order accurate Venkatakrishnan limiter is used. Roe's upwinding scheme without any entropy fix is employed for the flux function. Second-order central difference method is used for viscous flux. As a temporal integration method for steady calculations, implicit backward Euler scheme with restarted GMRES linear solver is employed. ILU(0) preconditioner is also used for the linear solver. All validation cases are converged to the extent that the residuals of all variables are reduced to 10^{-10}. For the baseline model, the "negative" formulation of the SA model (SA-neg) (Ref. 17) is used for all simulations conducted in this study.

Turbulent flat plate The 2D zero pressure gradient flat plate from the NASA turbulence modeling resource web page (Ref. 21) is selected as the first validation case. This case has a Mach number of 0.2 and a Reynolds number of 5 million. Five levels of structured grids available on the web page are utilized for the grid convergence study. More details regarding grid quality and boundary condition treatment can be found in (Ref. 21).

Grid convergence study results are shown in Fig. 4a. For comparison, CFL3D and FUN3D results are marked with dotted lines as well. CODA shows satisfactory performance in the grid convergence study. It nearly reaches the converged solution at the 4th grid, which has 69×49 points. SA-neg with production limiter results in acceptable convergence, and the difference from SA-neg is negligible. Distributions of skin friction coefficient in Fig. 4b and boundary layer profile in Fig. 4c also show identical results across all solvers.

Contours of TEV normalized by dynamic viscosity are presented in Fig. 5. As expected, both SA-neg with and without production limiter models show indistinguishable distributions. Small differences can be found at the edges of the boundary layer in Fig. 5c, but the relative difference compared to the maximum TEV is less than 0.2%. It is confirmed that c_1 and c_2 for the production limiter are properly determined.

Transonic airfoil: RAE2822 The second validation case is the RAE2822 airfoil of case 10, with a Mach number of 0.75 and an angle of attack of 2.81°. Experimental details can be found in (Ref. 22). O-type grids are constructed in a structured manner. 600 and 195 points are used for chordwise and normal directions, respectively. The first cell distance to the wall boundary is set to $y^+ = 1$.

The shock wave on the upper surface is well captured as shown in Fig. 6. Skin friction and pressure distributions are

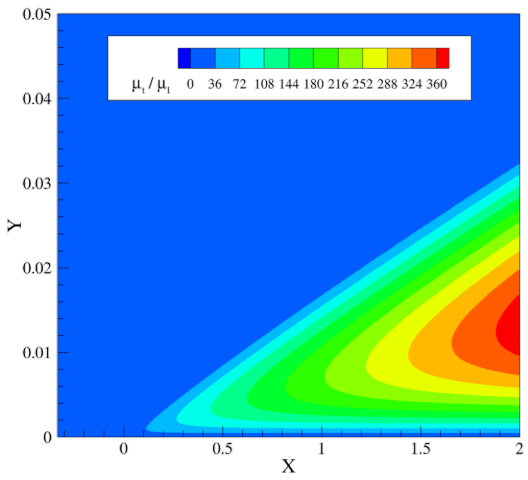

(a) SA-neg

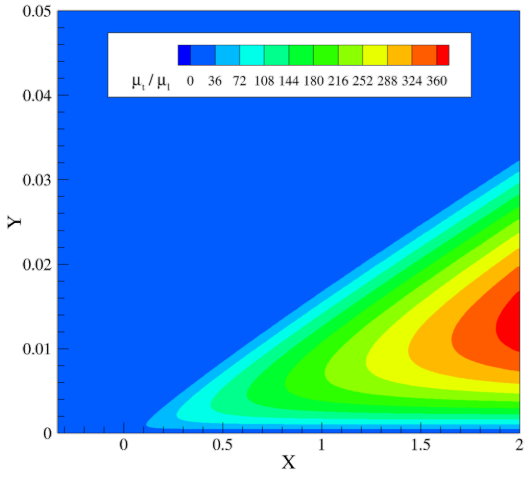

(b) SA-neg with production limiter

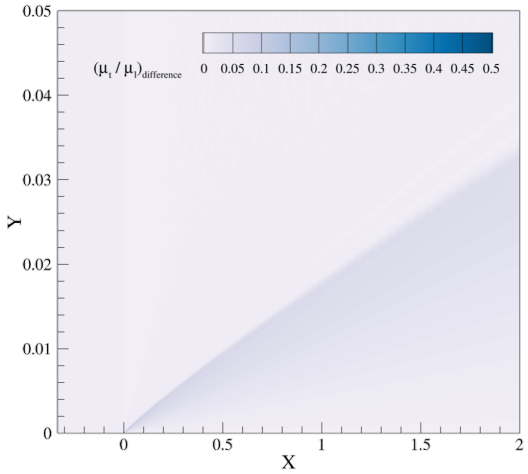

(c) Difference between SA-neg with and without production limiter

Figure 5. TEV contours for turbulent flat plate case.

well aligned with the experimental results. Velocity profiles within the boundary layer for four locations are presented in Fig. 7. Mild flow separation is observed at x/c = 0.65 where shock wave and boundary layer interaction occurs. There

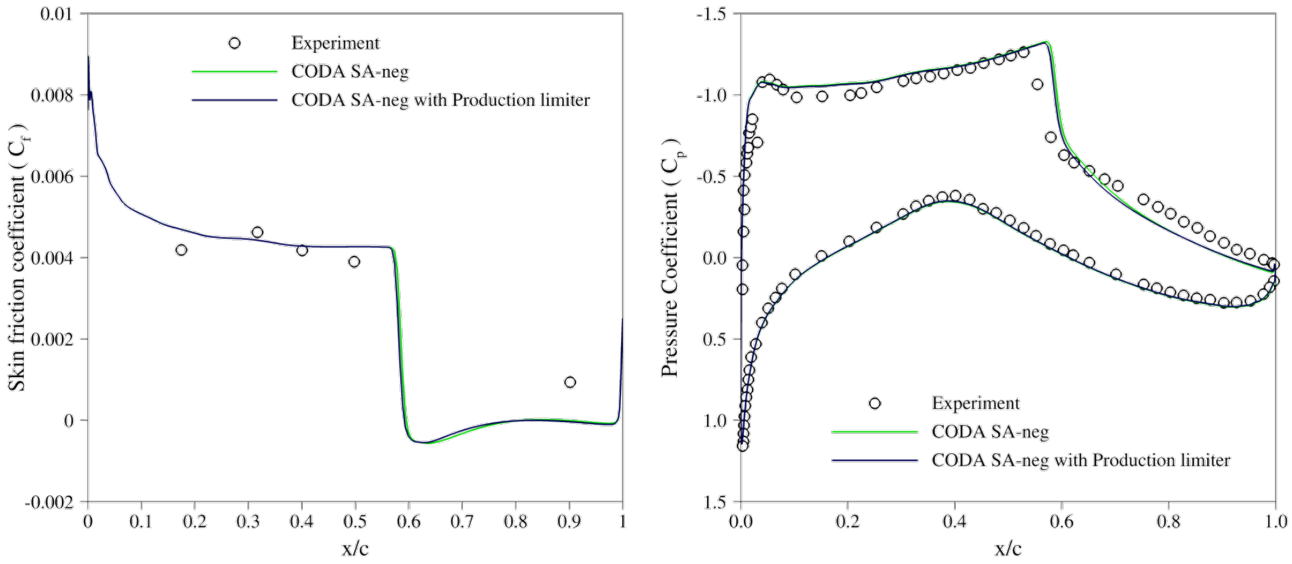

(a) Skin friction coefficient

(b) Pressure coefficient

Figure 6. Validation results for RAE2822 Airfoil with transonic condition.

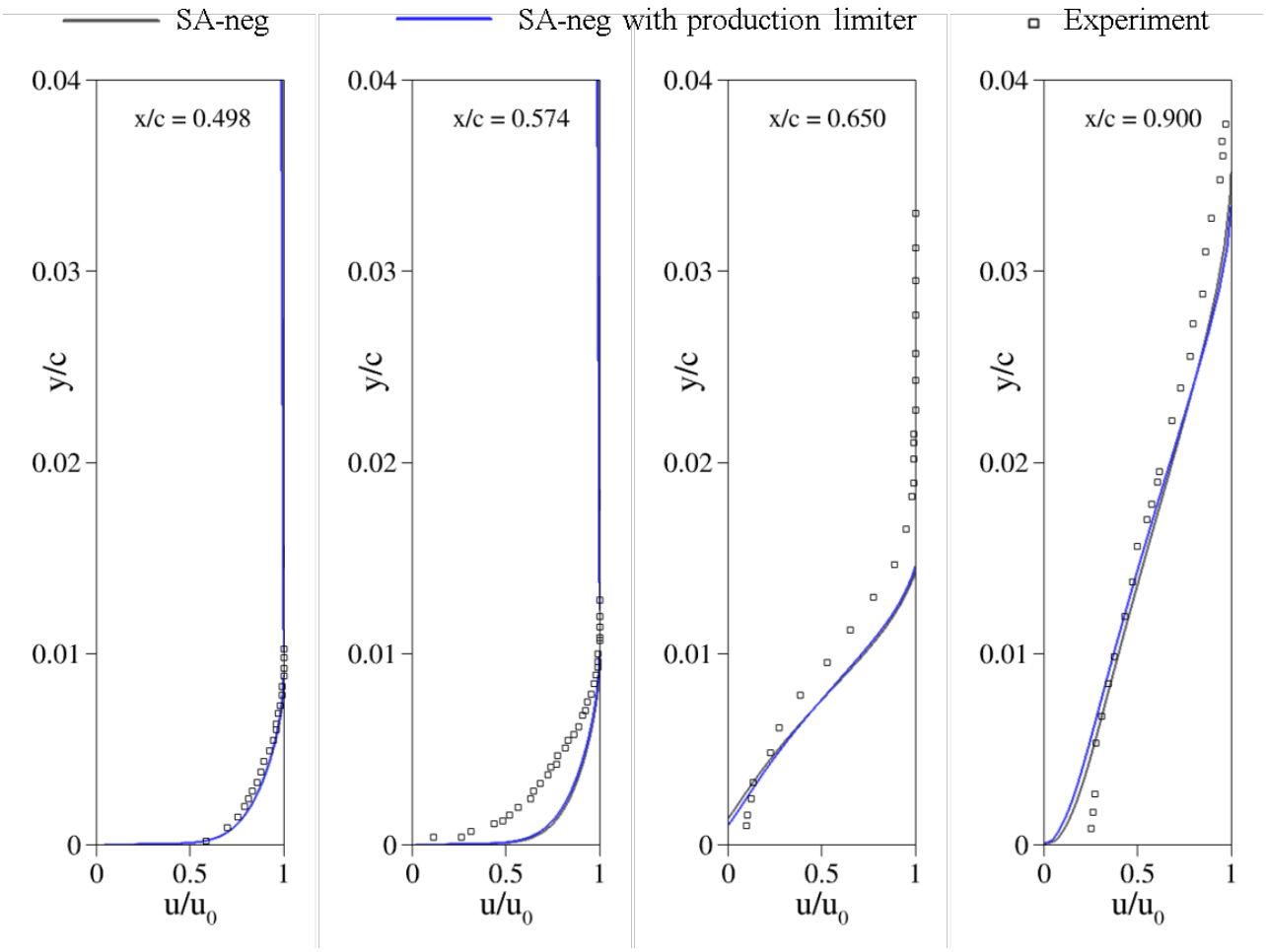

Figure 7: Velocity profiles for RAE2822 Airfoil with transonic condition.

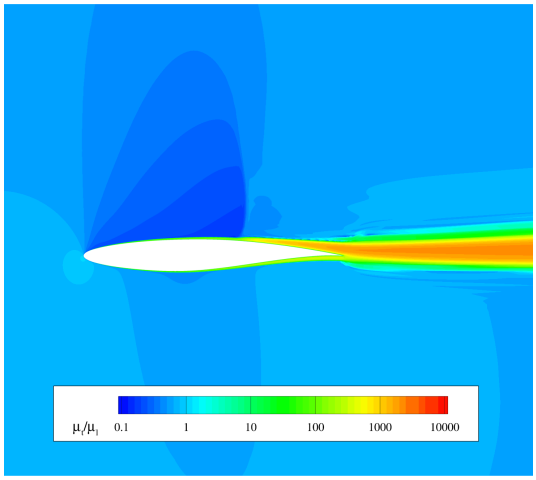

(a) SA-neg

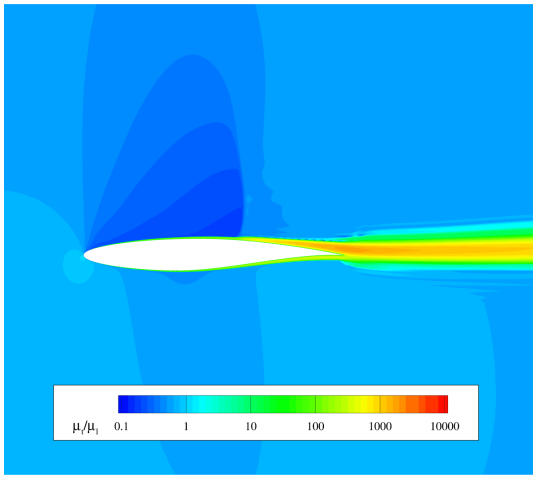

(b) SA-neg with production limiter

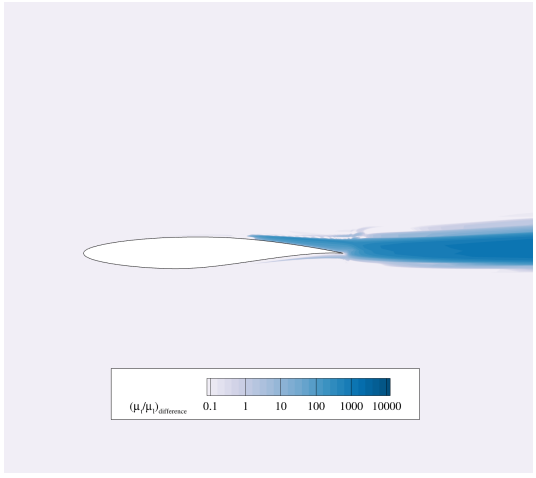

(c) Difference between SA-neg with and without production limiter

Figure 8. TEV contours for RAE2822 airfoil with transonic condition.

are some discrepancies between the experimental results and CODA results. However, the velocity profiles obtained using the SA-neg model with and without the production limiter exhibit negligible differences. It is verified that the current form

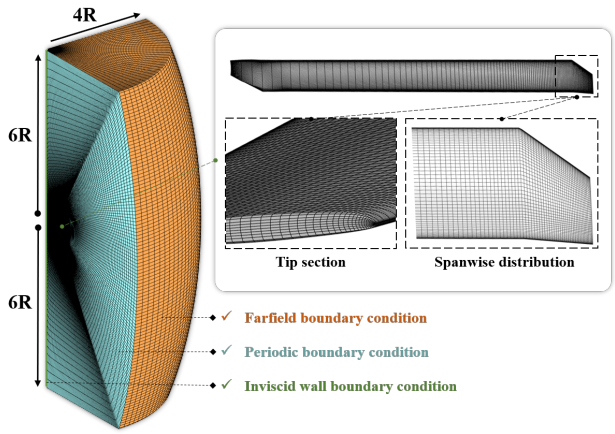

Figure 9. Monocoque grid for HVAB rotor.

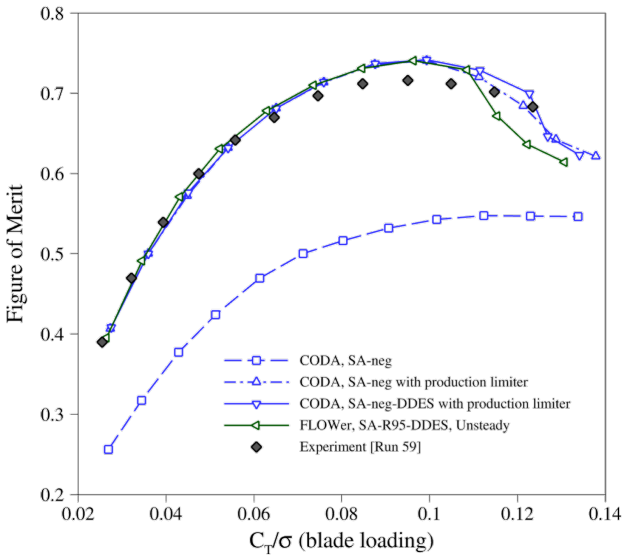

Figure 10. FM polar for HVAB rotor.

of production limiter has minimal impact on the boundary layer velocity profile.

TEV contours for CODA results are shown in Fig. 8. TEV is normalized by dynamic viscosity. Both models show similar distributions near-body region. Differences in TEV are noticeable in the wake region as can be seen in Fig. 8c. A significant amount of TEV is limited by the production limiter. It is noteworthy that the limited TEV does not change the behavior of fluids in the near-wall region. The velocity profile at x/c=0.9 in Fig. 7 presents small discrepancy, but ultimately skin friction and pressure coefficients remain the same. Therefore, it can be concluded that the original SA model without any limiter produces TEV excessively, indicating clear potential for improvement.

APPLICATION TO A HOVERING ROTOR

The HVAB rotor is employed to evaluate the effectiveness of the production limiter. This rotor is a widely recognized baseline configuration for hovering test cases, with extensive experimental data available across a spectrum of flow regimes,

from free-transition to fully turbulent conditions. Detailed rotor geometry and setup information can be found in (Ref. 15). Among the available data, Run59 — conducted under fully turbulent conditions with a tip Mach number of 0.65 and a tip Reynolds number of 2.14 million — is selected for this study. Aeroelastic effects are not considered; however, pre-defined coning (β) and lag (η) angles with hinge constraints are included. An isolated rotor configuration is adopted.

Grid and Solver Details

As this study focuses on steady-state simulations, a monocoque-type structured grid is employed, as illustrated in Fig. 9. The in-house grid generator G^3 (Ref. 23) is used to create the mesh. An O–O type blade grid is first generated and then extruded to form a truncated cylindrical domain, resembling a sliced cake. The grid consists of approximately 2.7 million points. The first-cell height from the blade wall is set to achieve a normalized wall distance of y^+ close to 1. Periodic, far-field, and inviscid wall boundary conditions are applied on the corresponding surfaces shown in Fig. 9.

A rotating reference frame accounting for Coriolis effects is used. Most aspects of the spatial and temporal integration methods follow those used in the validation cases, with two notable differences: 1) An entropy fix is applied to the Roe scheme to improve robustness, and 2) The convergence criterion is set to 10^{-8}. The strong linear solver in CODA allows

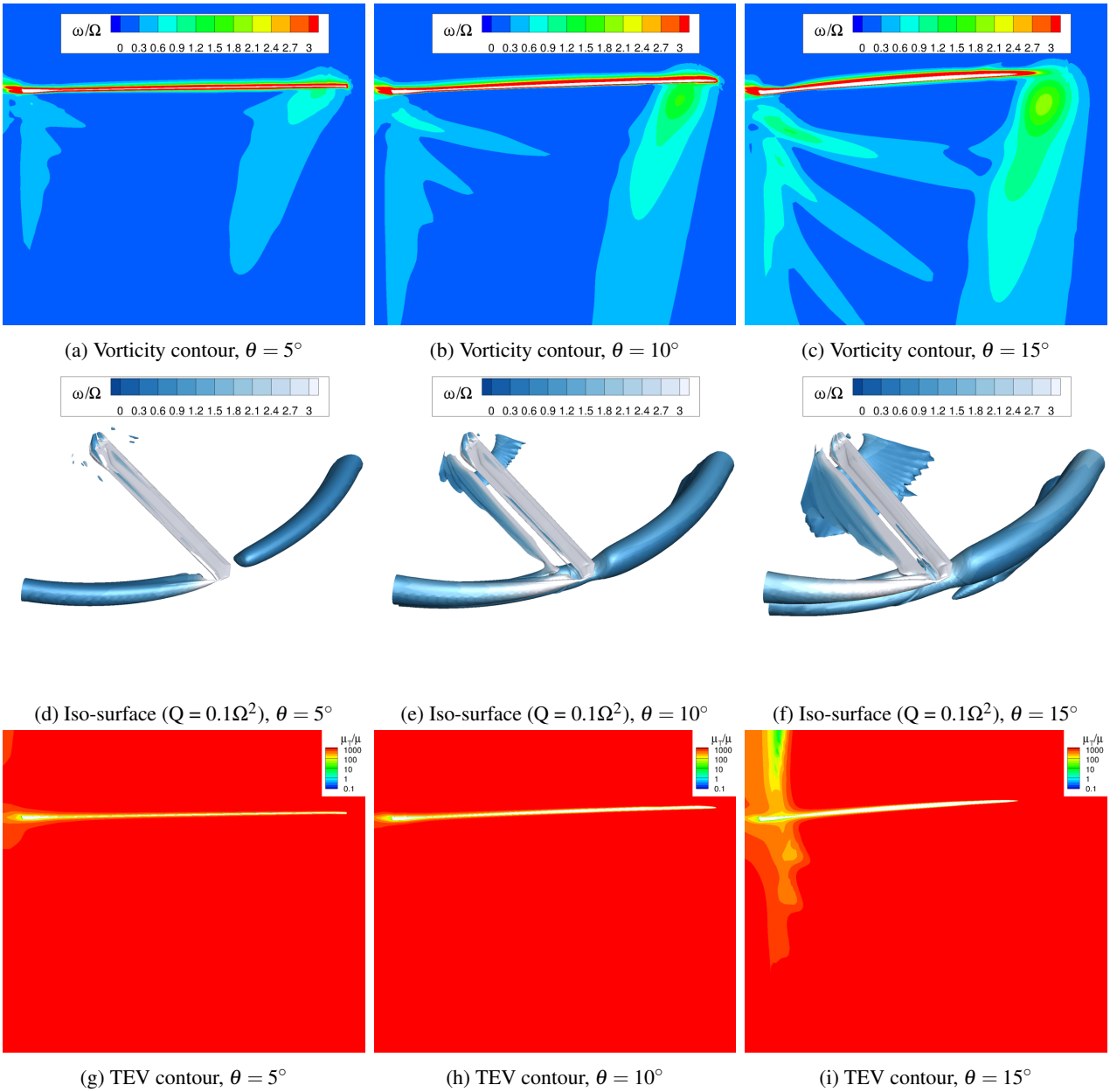

(a) Vorticity contour, $\theta = 5°$ (b) Vorticity contour, $\theta = 10°$ (c) Vorticity contour, $\theta = 15°$

(d) Iso-surface ($Q = 0.1\Omega^2$), $\theta = 5°$ (e) Iso-surface ($Q = 0.1\Omega^2$), $\theta = 10°$ (f) Iso-surface ($Q = 0.1\Omega^2$), $\theta = 15°$

(g) TEV contour, $\theta = 5°$ (h) TEV contour, $\theta = 10°$ (i) TEV contour, $\theta = 15°$

Figure 11. HVAB simulation results using SA-neg model. Vorticity contour, Iso-surfaces of Q-criterion, and TEV contours for three collective pitch angles are presented.

convergence of the HVAB rotor case to near machine accuracy. However, once the solution converges to a certain threshold, further reduction in residuals yields negligible changes in thrust and torque. Thus, the convergence threshold can be relaxed for saving some computing cost. Most cases converge to a density residual of 10^{-8} within 6,000 iterations. In cases where the residual oscillates, force coefficients remain flat, indicating practical convergence.

Results and Discussion

Figure 10 presents the Figure of Merit (FM) polar for the HVAB rotor. For comparison, results from the block-structured CFD solver - FLOWer are included. The same grid as the one for CODA is used. Advanced solver settings (Ref. 24) are used for FLOWer: 1) unsteady simulations with SA-neg-DDES-R95 model, and 2) the SLAU2 all-speed convective flux scheme (Ref. 25) combined with a fourth-order Van Albada limiter (Ref. 26). FLOWer simulations are run for up to 50 revolutions to achieve fully developed wake structures and stable force coefficients. The final revolution is time-averaged to obtain integrated aerodynamic performance.

CODA results are shown as blue lines in Fig. 10. The SA-neg model significantly underpredicts FM compared to other CFD results and experimental data, primarily due to excessive TEV growth. In contrast, the SA-neg model with the production limiter yields substantially improved FM predictions.

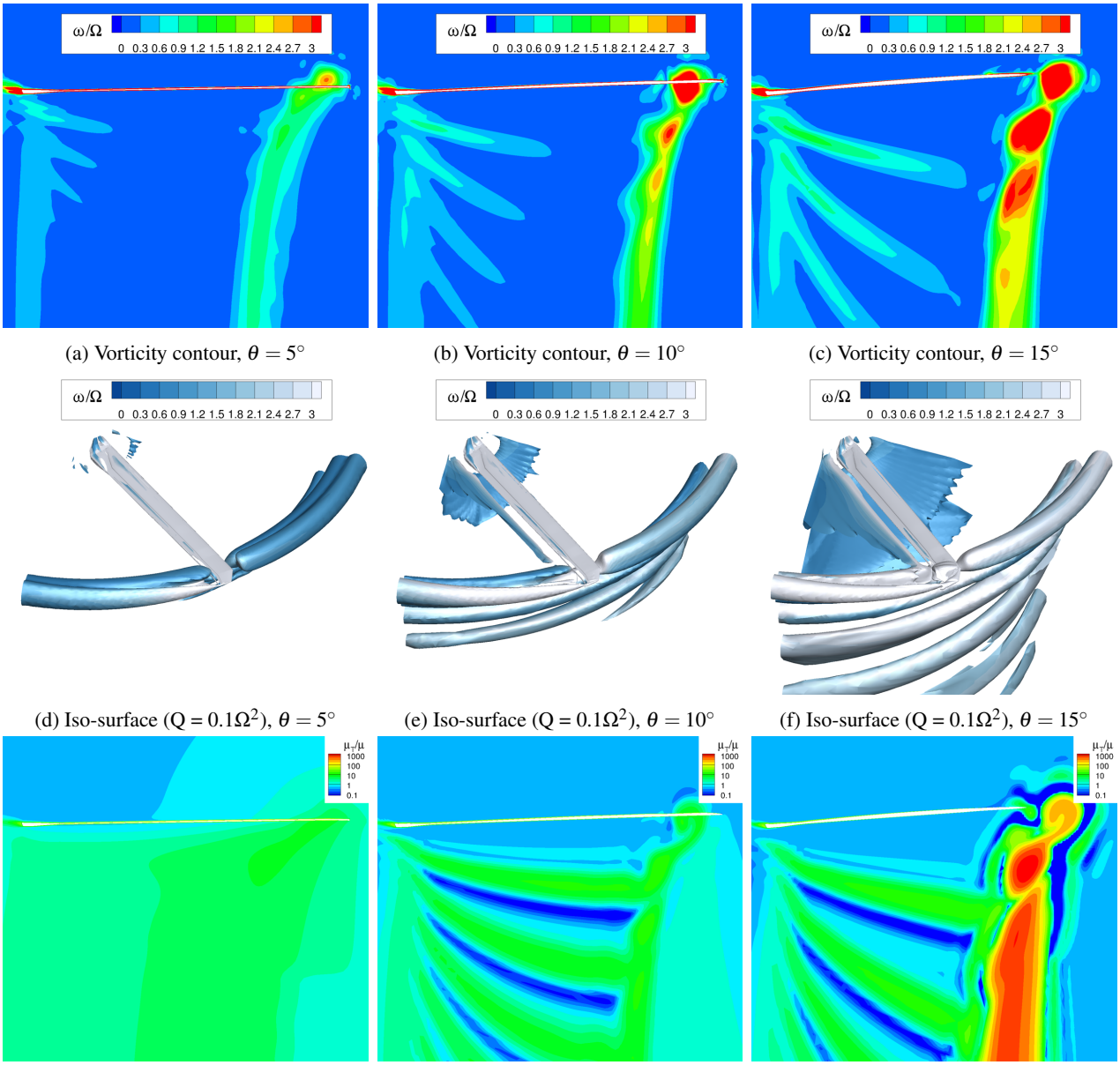

(a) Vorticity contour, $\theta = 5°$ (b) Vorticity contour, $\theta = 10°$ (c) Vorticity contour, $\theta = 15°$

(d) Iso-surface ($Q = 0.1\Omega^2$), $\theta = 5°$ (e) Iso-surface ($Q = 0.1\Omega^2$), $\theta = 10°$ (f) Iso-surface ($Q = 0.1\Omega^2$), $\theta = 15°$

(g) TEV contour, $\theta = 5°$ (h) TEV contour, $\theta = 10°$ (i) TEV contour, $\theta = 15°$

Figure 12. HVAB simulation results using SA-neg model with production limiter. Vorticity contour, Iso-surfaces of Q-criterion, and TEV contours for three collective pitch angles are presented.

The limiter effectively suppresses TEV escalation, leading to results that align closely with the unsteady DDES simulations with FLOWer, which also avoid excessive TEV.

The SA-neg-DDES model combined with the production limiter is also evaluated for this configuration. In this case, the limiter is applied after modifying the destruction term according to the DDES formulation. As seen in the FM polar, this DDES version also agrees with the other CFD results and experimental values up to a blade loading coefficient of 0.1. Beyond this point, in the post-stall region, none of the CFD models align well with the experiments. The flow becomes highly unsteady and increasingly sensitive to TEV behavior. A large separation bubble forms near the outer blade region, posing a continued challenge for accurate numerical prediction.

Flow fields computed using SA-neg and SA-neg with the production limiter are presented in Fig. 11 and Fig. 12, respectively. Each column corresponds to a different collective pitch angle, while each row shows vorticity contours, Q-criterion iso-surfaces, and TEV contours. Vorticity is normalized by the angular velocity, and TEV is normalized by the dynamic viscosity. As reflected in the FM polar, the SA-neg model produces excessively high TEV, resulting in highly dissipative flow fields. Vortices are rapidly diffused, losing their strength and coherence. Consequently, tip vortices merge into a large, smeared-out structure that engulfs the outer region of the rotor blade across all pitch angles.

In contrast, the SA-neg model with the production limiter consistently suppresses TEV growth for all pitch angles, as shown in Fig. 12. Except for the tip vortex trajectory at a pitch angle of 15°, the TEV ratio in the wake remains below 10. The reduced TEV helps maintain high vorticity, as shown in the vorticity magnitude contours and iso-surfaces. Whereas the SA-neg model without a limiter produces one large, dissipated tip vortex, the production-limited version retains coherent vortices with high vorticity magnitudes. At a pitch angle of 5°, three tip vortices are distinctly captured. At 10° and 15°, more than five tip vortices are observed. These well-preserved vortices contribute to more accurate predictions of aerodynamic performance. Although not shown in this paper, the SA-neg-DDES model with the production limiter produces similar flow features to those in Fig. 12.

EXPERIMENTS ON MODEL COEFFICIENTS OF THE PRODUCTION LIMITER

A parametric study is conducted on the coefficients of the production limiter, c_1 and c_2, to understand their effective operating ranges. As introduced in the previous section, the coefficient c_1 represents the ratio of the production term to the destruction term in the SA model, directly controlling the upper limit of the production of SA variable. A larger c_1 value causes the modified model to behave more like the original SA model. Conversely, a lower c_1 enhances the limiting effect but may compromise solution accuracy and convergence due to insufficient TEV.

The coefficient c_2 is associated with the f_d term in the shielding function and determines the extent of the shielding region. Increasing c_2 enlarges the shielding zone, deactivating the production limiter over a broader area. Conversely, decreasing c_2 narrows the shielding region, thereby increasing the area where production is limited. If c_2 is set too low, the TEV required for accuracy and stability may not be sufficiently generated, which can lead to solver instability or even divergence. The recommended value in the SA-DDES model (Ref. 9) is 8; however, several studies have suggested higher values for more effective shielding (Refs. 18, 19, 27). Therefore, identifying appropriate c_2 values is crucial for activating the limiter in the correct flow regions.

Three representative test cases are used in this study: a turbulent flat plate, the RAE2822 airfoil, and the HVAB rotor. Contours shown in Fig. 13 illustrate the deviation between results obtained using the limiter and the ideal reference results. The dotted lines in the figure represent the simulation results. A total of 30 simulations were performed for each test configuration. The simulation parameters were determined using a full factorial design, with c_1 values of $10^1, 10^2, 10^3, 10^4, 10^6, 10^8$, and c_2 values of $0, 8, 20, 40, 100$. For the flat plate and RAE2822 cases, the solution from SA-neg without any limiter is used as the reference. Performance is assessed using L_1 error in skin friction. For the HVAB rotor, where the original SA-neg model suffers from excessive TEV, the ideal reference is obtained from an unsteady simulation using CODA with SA-neg-R95-DDES model. This simulation employs the same grid and numerical setup, with the turbulence model as the only difference. Physical time stepping is carried out using SDIRK22, with a time advancement of 0.5° per step. A total of 50 rotor revolutions are simulated, and results from the final revolution are time-averaged to compute the FM.

The contour results for the flat plate (Fig. 13a) and RAE2822 (Fig. 13b) are nearly indistinguishable. In both cases, the production limiter has negligible effect on aerodynamic performance, except for a minor region in the lower-left corner. Notably, even when the limiter is active across the entire domain including within the boundary layer ($c_2 = 0$), its impact remains minimal as long as $c_1 \geq 100$. Conversely, even when the production term is limited to a low ratio (e.g., $c_1 = 10$), shielding the boundary layer effectively using a high c_2 value prevents degradation in performance.

For the HVAB rotor, some discrepancies emerge for values $c_1 > 10^6$. The original formulation of SA is recovered for large c_1 value. The increased TEV dissipates tip vortices near the rotor blade, thereby compromising the accuracy of performance predictions.

Based on these experiments, suitable ranges for the model coefficients can be recommended as:

$$10^2 \leq c_1 \leq 10^6, \quad 20 \leq c_2 \leq 100.$$

To reduce computational cost, a simplified limiter across the entire domain without shielding may also be used:

$$10^2 \leq c_1 \leq 10^6, \quad c_2 = 0.$$

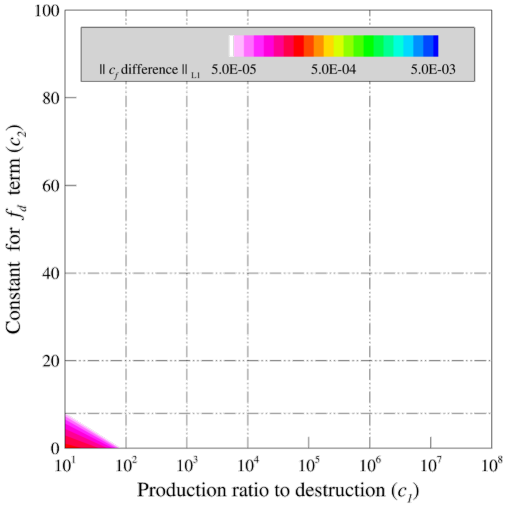

(a) Turbulent flat plate, difference of skin friction

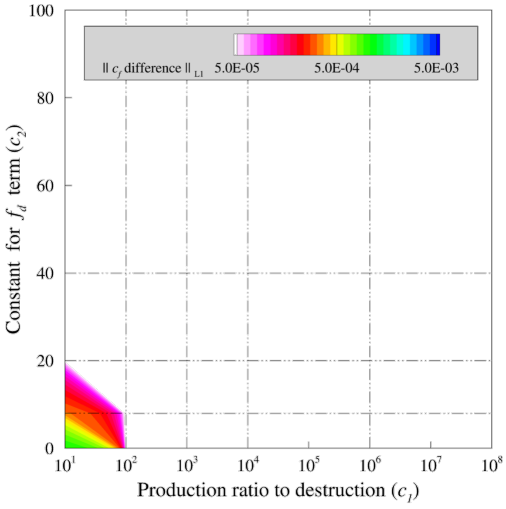

(b) RAE2822 airfoil, difference of skin friction

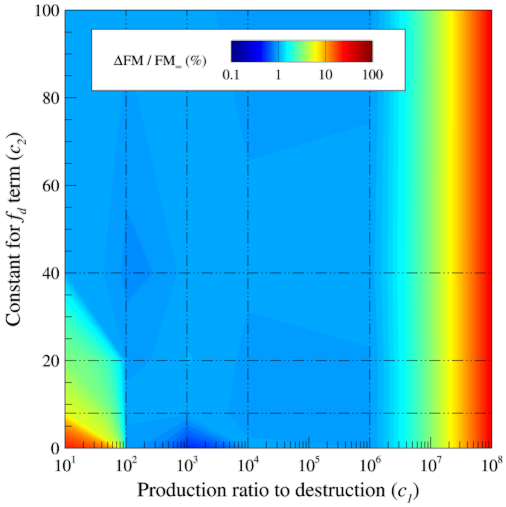

(c) HVAB rotor, difference of FM

Figure 13. Parameter study results for the two coefficients of the production limiter. Grids with the dashed line represents the data points that are solved.

However, it should be noted that the current formulation of the production limiter has only been validated for hovering rotors and simple test cases. Caution is advised when applying it to complex flow scenarios, such as those involving large scale separation at high angles of attack or multi-element airfoils, and such applications should be supported by further case-specific validation.

CONCLUSIONS

A production limiter for suppressing the growth of the SA variable in the wake region is introduced to obtain reliable converged solutions in hovering flow fields. This production limiter is evaluated across various test cases, including flat plate, airfoil, and hovering rotor configurations. The key findings are as follows:

1. The present production limiter is designed to mitigate the problem of excessive increases in TEV within hovering flow fields. It is formulated to suppress the production term of the SA variable to a ratio of the destruction term. Recognizing that the original SA model is calibrated for boundary layer regions, the limiter incorporates a shielding function from the DDES formulation to avoid limiting the production term within the boundary layer. Validation results from turbulent flat plate and transonic airfoil cases demonstrate that this limiter deactivates within the boundary layer while suppressing production in the wake region. Furthermore, it is shown that the suppressed TEV resulting from the limiter has negligible impact on aerodynamic performance for the examined test cases.

2. The problem of unbounded TEV accumulation in hovering flow fields is effectively resolved through the utilization of the production limiter. HVAB rotor results indicate that the limiting technique successfully suppresses TEV throughout the entire wake region, consequently enhancing vorticity preservation and, therefore, the accuracy of aerodynamic performance predictions. The DDES approach can also be combined with this limiter, yielding satisfactory results for performance prediction. As a result, the production limiter enables improved aerodynamic performance predictions using a steady solver. Considering that such predictions typically require unsteady solvers, this approach proves to be highly cost-effective.

3. The applicable range of model coefficients is established through systematic experiments across three test cases. Simple test cases, including flat plate and transonic airfoil configurations, demonstrate that a wide range of coefficients produces acceptable results, except in the narrow region where c_1 and c_2 are below 100 and 20, respectively. In this limited region, the production limiter suppresses TEV excessively, resulting in degraded accuracy and robustness of the SA model. HVAB rotor tests show that coefficient ranges of $10^2 - 10^6$ for c_1 and $20 - 100$ for c_2 yield feasible results for performance prediction.

When c_1 becomes excessively large, the predictions approach those of the original SA model, indicating that the limiter is no longer activated in the wake region and cannot suppress TEV growth.

The proposed production limiter represents a practical and robust approach to addressing the challenge of excessive TEV in hovering rotorcraft simulations. By preserving the original SA model formulation within boundary layers while selectively suppressing production in wake regions, the modified model demonstrates improved vortex preservation and enhanced predictive accuracy with minimal computational overhead. Future work may explore the extension of this approach to more complex rotorcraft configurations.

ACKNOWLEDGMENTS

The authors gratefully acknowledge the scientific support and HPC resources provided by the German Aerospace Center (DLR). The HPC system CARA is partially funded by "Saxon State Ministry for Economic Affairs, Labour and Transport" and "Federal Ministry for Economic Affairs and Climate Action".

REFERENCES

1. Chaderjian, N. M., "Quantitative Approach for the Accurate CFD Simulation of Hover in Turbulent Flow," The 11th International Conference on Computational Fluid Dynamics, 2022.

2. Stefanin Volpiani, P., Chapelier, J.-B., Schwöppe, A., Jägersküpper, J., and Champagneux, S., "Aircraft simulations using the new cfd software from onera, dlr, and airbus," *Journal of Aircraft*, Vol. 61, (3), 2024, pp. 857–869.

3. Wilke, G., and Gerlach, R., "Maximum thrust studies of an isolated rotor with CFD turbulence modelling and grid sensitivities," 51st European Rotorcraft Forum, 2025.

4. Richez, F., and Jain, R., "Prediction of the laminar-to-turbulent transition position on a helicopter rotor in forward flight," 50th European Rotorcraft Forum (ERF 2024), 2024.

5. Kim, Y., Hong, Y., Shon, S., Kang, Y.-E., and Yee, K., "A Simulation Framework for Performance and Safety Evaluation of a Hovering Rotor in Icing Conditions," AIAA AVIATION FORUM AND ASCEND 2024, 2024.

6. Park, D., and Park, S. H., "Effect of Jet–Wake Interaction around a Tip-Jet Rotor in Torque-Balanced States," *International Journal of Aeronautical and Space Sciences*, Vol. 25, (3), 2024, pp. 922–932.

7. Dacles-Mariani, J., Zilliac, G. G., Chow, J. S., and Bradshaw, P., "Numerical/experimental study of a wingtip vortex in the near field," *AIAA journal*, Vol. 33, (9), 1995, pp. 1561–1568.

8. Alauzet, F., and Spalart, P., "A new rotation correction for the Spalart-Allmaras model to improve off-body vortex prediction and vortex-vortex interaction effects," AIAA SCITECH 2024 Forum, 2024.

9. Spalart, P. R., Deck, S., Shur, M. L., Squires, K. D., Strelets, M. K., and Travin, A., "A new version of detached-eddy simulation, resistant to ambiguous grid densities," *Theoretical and computational fluid dynamics*, Vol. 20, 2006, pp. 181–195.

10. Spalart, P. R., "Detached-eddy simulation," *Annual review of fluid mechanics*, Vol. 41, (1), 2009, pp. 181–202.

11. Travin, A. K., Shur, M. L., Spalart, P. R., and Strelets, M. K., "Improvement of delayed detached-eddy simulation for LES with wall modelling," ECCOMAS CFD 2006: Proceedings of the European Conference on Computational Fluid Dynamics, Egmond aan Zee, The Netherlands, September 5-8, 2006, 2006.

12. Potsdam, M., and Pulliam, T., "Turbulence modeling treatment for rotorcraft wakes," AHS Specialist's Conference on Aeromechanics, 2008.

13. Yoon, S., Chaderjian, N., Pulliam, T. H., and Holst, T., "Effect of turbulence modeling on hovering rotor flows," 45th AIAA Fluid Dynamics Conference, 2015.

14. Norman, T. R., Heineck, J. T., Schairer, E. T., Schaeffler, N. W., Wagner, L. N., Yamauchi, G. K., Overmeyer, A. D., Ramasamy, M., Cameron, C. G., Dominguez, M., *et al.*, "Fundamental Test of a Hovering Rotor: Comprehensive Measurements for CFD Validation," Vertical Flight Society's 79th Annual Forum & Technology Display, 2023.

15. "AIAA Rotorcraft Hover Prediction Workshop (HPW)," http://www.aiaa-hpw.org, Accessed: 2025.07.10.

16. Spalart, P., and Allmaras, S., "A one-equation turbulence model for aerodynamic flows," 30th aerospace sciences meeting and exhibit, 1992.

17. Allmaras, S. R., and Johnson, F. T., "Modifications and clarifications for the implementation of the Spalart-Allmaras turbulence model," Seventh international conference on computational fluid dynamics (ICCFD7), Vol. 1902, 2012.

18. Jain, N., and Baeder, J. D., "Assessment of shielding parameters in conventional DDES method under the presence of alternative turbulence length scales," 23rd AIAA Computational Fluid Dynamics Conference, 2017.

19. Letzgus, J., *High-fidelity simulation of dynamic stall on helicopter rotors*, Ph.D. thesis, Dissertation, Stuttgart, Universität Stuttgart, 2021, 2021.

20. Schwöppe, A., and Diskin, B., "Accuracy of the cell-centered grid metric in the DLR TAU-code," New Results in Numerical and Experimental Fluid Mechanics VIII: Contributions to the 17th STAB/DGLR Symposium Berlin, Germany 2010, 2013.

21. NASA Langley Research Center, "NASA Turbulence Modeling Resource," https://turbmodels.larc.nasa.gov/, Accessed: 2025.07.10, 2025.

22. Cook, P. H., McDonald, M. A., and Firmin, M. C. P., "Aerofoil RAE 2822 - Pressure distributions and boundary layers and wake measurement," AGARD, Advisory Rept. 138-A6, 1979.

23. Wilke, G., "Successive Optimization of Airfoils, Planform and Twist for Aerodynamic Performance of Helicopter Rotor Blades," Vertical Flight Society 79th Annual Forum and Technology Display, 2021.

24. Wilke, G., Bailly, J., Kimura, K., and Tanabe, Y., "JAXA-ONERA-DLR cooperation: results from rotor optimization in hover," *CEAS Aeronautical Journal*, Vol. 13, (2), 2022, pp. 313–333. DOI: https://doi.org/10.1007/s13272-022-00580-8.

25. Kitamura, K., and Shima, E., "Towards shock-stable and accurate hypersonic heating computations: A new pressure flux for AUSM-family schemes," *Journal of Computational Physics*, Vol. 245, 2013, pp. 62–83.

26. Wilke, G., "Comparisons of different spatial schemes and limiters for helicopter flows," New Results in Numerical and Experimental Fluid Mechanics XIII: Contributions to the 22nd STAB/DGLR Symposium, 2021.

27. Probst, A., Wolf, C., Radespiel, R., Knopp, T., Schwamborn, D., and Radespiel, R., "A comparison of detached-eddy simulation and Reynolds-stress modeling applied to the flow over a backward-facing step and an airfoil at stall," 48th AIAA aerospace sciences meeting including the New horizons forum and aerospace exposition, 2010.